Interplay of local structure, charge, and spin in bilayered manganese perovskites

Damian Rybicki,[1,*] Marcin Sikora,[2,†] Janusz Przewoznik,[1] Czesław Kapusta,[1] and John F. Mitchell[3]
[1]*AGH University of Science and Technology, Faculty of Physics and Applied Computer Science, Department of Solid State Physics, al. A. Mickiewicza 30, 30-059 Krakow, Poland*
[2]*AGH University of Science and Technology, Academic Centre for Materials and Nanotechnology, al. A. Mickiewicza 30, 30-059 Krakow, Poland*
[3]*Argonne National Laboratory, Materials Science Division, Argonne, Illinois 60439, USA*

(Received 10 November 2017; revised manuscript received 14 February 2018; published 27 March 2018)

Chemical doping is a reliable method of modification of the electronic properties of transition metal compounds. In manganese perovskites, it leads to charge transfer and peculiar ordering phenomena. However, depending on the interplay of the local crystal structure and electronic properties, synthesis of stable compounds in the entire doping range is often impossible. Here, we show results of high-energy resolution x-ray absorption and emission spectroscopies on a $La_{2-2x}Sr_{1+2x}Mn_2O_7$ family of bilayered manganites in a broad doping range ($0.5 \leqslant x \leqslant 1$). We established a relation between local Mn charge and Mn-O distances as a function of doping. Based on a comparison of such relation with other manganites, we suggest why stable structures cannot be realized for certain doping levels of bilayered compounds.

DOI: 10.1103/PhysRevB.97.115158

I. INTRODUCTION

Mixed-valent manganese perovskites show a plethora of types of magnetic, charge, and orbital orders, which occur due to interplay of various degrees of freedom including spin, charge, and the lattice. Adding chemical doping, temperature, or external pressure as parameters leads to even more complicated phase diagrams, but it also allows for tuning their properties to those required for the given application, e.g., in spintronics, catalysis, or solar energy-to-fuel conversion [1,2]. The most extensively studied are manganites with a pseudocubic perovskite structure of the general formula $R_{1-x}A_xMnO_3$, where R and A are a trivalent and divalent cation, respectively. These compounds have strongly distorted and rotated MnO_6 octahedra with Mn-O-Mn bond angles varying between 155–170°. There are, however, families without tilted octahedra such as $La_{1-x}Sr_{1+x}MnO_4$ (called single layered as it has a single MnO_2 layer in the unit cell) and the least distorted $La_{2-2x}Sr_{1+2x}Mn_2O_7$ (called bilayered). Both families have tetragonal structure and typical Mn-O-Mn angles are close to 180° [3]. $La_{2-2x}Sr_{1+2x}Mn_2O_7$ family in the doping range $0.5 \leqslant x \leqslant 1$ shows most clearly the connection between orbital ordering and magnetism [3]. The doping, in accordance with Goodenough's rules, leads to less ferromagnetism, which was also concluded from our nuclear magnetic resonance experiments on samples in the same doping range [4].

To study the interplay between the local crystal structure and the electronic properties in detail, we used x-ray absorption and emission spectroscopy (XAS and XES, respectively) as they are sensitive to the local structure, spin, and charge [5]. Pseudocubic perovskites have been extensively studied using XAS and core-level XES [5–11] for more than 20 years. However, due to recent advances in high-resolution hard x-ray photon-in photon-out spectroscopy [12], background-free XAS and valence-band XES can be probed giving access to even more details on the hybridization and evolution of electronic bands near the Fermi level. Therefore, our goal is to examine the role of the local structure as well as to gain insight into the electronic structure of bilayered manganites using XAS and XES techniques. Since there exist similar studies on the pseudocubic $La_{1-x}Sr_xMnO_3$ and single layer $La_{1-x}Sr_{1+x}MnO_4$ families, we can now compare them to our results to make more general conclusions for all manganites. In contrast to pseudocubic $La_{1-x}Sr_xMnO_3$, at room temperature, compounds from the $La_{2-2x}Sr_{1+2x}Mn_2O_7$ family have the same type of crystal structure and no orbital/charge/magnetic orders are present, even though their influence on the XES/XAS spectra in pseudocubic compounds was shown to be rather weak [13]. While general trends obtained from near edge x-ray absorption structure (XANES) are similar in all the three families, e.g., evolution of the prepeak area and the edge energy with doping, there are also differences in terms of values of the chemical shift. XES measurements show even more significant differences and indicate that in the $La_{2-2x}Sr_{1+2x}Mn_2O_7$ family, Mn spin changes linearly with doping, which is in contrast to $La_{1-x}Sr_{1+x}MnO_4$. Results of XES and XAS measurements appear to be tied to Mn-O distances in MnO_6 octahedra and our findings shine more light on the reasons why bilayered manganites cannot be synthesized in the entire doping range.

II. EXPERIMENTAL

Polycrystalline samples of $La_{2-2x}Sr_{1+2x}Mn_2O_7$ (for $x =$ 0.5, 0.62, 0.68, 0.75, 0.8, and 1) were prepared by the high-temperature solid state reaction method [14]. Powder XRD

*ryba@agh.edu.pl
†marcins@agh.edu.pl

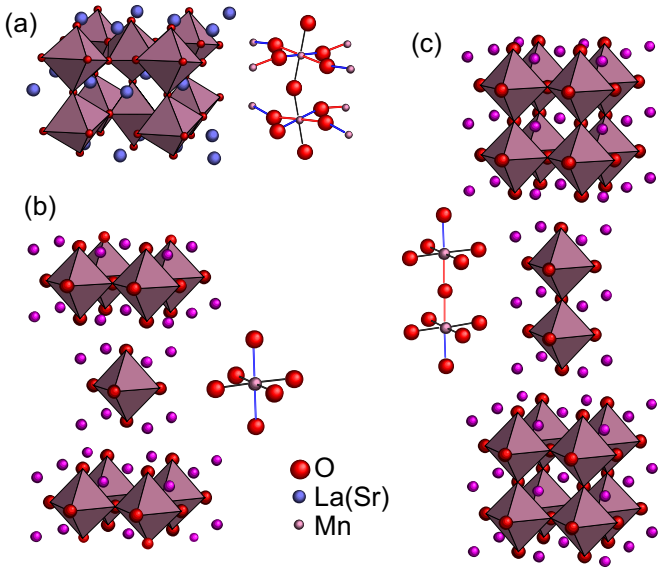

FIG. 1. Crystal structure of (a) "pseudocubic" $LaMnO_3$, (b) single-layer $La_{1-x}Sr_{1+x}MnO_4$, and (c) bilayered $La_{2-2x}Sr_{1+2x}Mn_2O_7$ with corresponding arrangements of MnO_6 octahedra. Different colors of Mn-O bonds indicate different lengths.

measurements showed that samples are single phase (see the Supplemental Material [15] and supplemental Fig. 1). The x-ray absorption and $K\beta$ emission spectra of the Mn K-edge were collected at the ID26 beamline of the European Synchrotron Radiation Facility in Grenoble, France. The undulator fundamental monochromatized by a pair of Si(311) crystals and an emission spectrometer in Rowland circle geometry equipped with Si(440) analyzer crystal were used. The total energy resolution of the setup, measured as full width at half maximum of the elastic profiles, was determined to be ≈0.7 eV. The reproducibility of the monochromator and spectrometer energy was better than ≈0.05 eV. X-ray absorption spectra were probed using the total fluorescence yield (TFY) and the high-energy resolution fluorescence detection (HERFD) [12]. The latter were measured by probing the maximum intensity of the $K\beta$ fluorescence line. Such $1s3p$ HERFD XANES shows significantly better resolved spectral features compared to Mn K-edge TFY-XANES, particularly in the pre- and near-edge range (see the Supplemental Material [15] and supplemental Fig. 3). Therefore, the analysis of the spectral shape evolution is based on HERFD data. Quantitative determination of the edge energy is derived from the maximum of the first derivative of TFY-XANES to compare our results with those obtained for other manganites.

X-ray emission spectra were taken at 6900 eV incident energy over the energy span covering both core-to-core (CTC) transitions corresponding to $K\beta_{1,3}$ main line and $K\beta'$ satellite as well as the valence-to-core (VTC) transitions corresponding to $K\beta_{2,5}$ and Kβ'' features. All measurements were carried out at room temperature. The Mn $K\beta$ XES spectra have been normalized to the area within the emission energy range 6467–6512 eV. The Mn $K\beta$ VTC region spectra have been further smoothed over 1.5 eV window using moving average algorithm. HERFD and TFY XANES spectra have been normalized to the unity mean value in the energy range 6660–6650 eV with respect to the pre-edge region.

For plot clarity, we do not present data for all samples in figures presenting the results of measurements; however, plots showing dependencies as a function of doping or distances include results for all the samples studied.

III. RESULTS

At room temperature, all $La_{2-2x}Sr_{1+2x}Mn_2O_7$ compounds are paramagnetic insulators and have a tetragonal crystal structure with three different Mn-O bond lengths ($d_{Mn\text{-}O}$) within a bilayer [16]. By symmetry, all distances between Mn and equatorial O3 are the same, but there are two different distances to apical oxygens (O1 and O2) as shown in Fig. 1. Single-layer $La_{1-x}Sr_{1+x}MnO_4$ has tetragonal structure, as well, but the distances between Mn and apical oxygens are the same. "Pseudocubic" $LaMnO_3$ has different distortion of MnO_6 octahedra (two significantly different Mn-O equatorial bond lengths while the distance between Mn and apical oxygen is very similar to the shorter equatorial one), which are additionally tilted. In Fig. 2, we present the doping dependencies of all Mn-O distances from neutron diffraction [16]. We observe that the average Mn-O distance $< d_{Mn-O} >$ monotonically decreases with Sr (hole) doping as expected, since the average ionic size of Mn decreases with increase of its formal valence state. Similar decrease of $< d_{Mn-O} >$ was observed for $La_{1-x}Sr_xMnO_3$ [17] and $La_{1-x}Sr_{1+x}MnO_4$ [18]. The distortion of MnO_6 octahedra in $La_{2-2x}Sr_{1+2x}Mn_2O_7$ is much smaller compared to $LaMnO_3$ or $La_{1-x}Sr_{1+x}MnO_4$ (see the Supplemental Material [15] and supplemental Fig. 2).

Now we turn to results of synchrotron measurements. Based on structural parameters obtained from diffraction measurements, we model the evolution of Mn K-edge spectra by means of FDMNES calculations [19] (for more details see the supplement [15] and supplemental Fig. 4). They show significant shift of the main edge between $LaMnO_3$ and $La_{2-2x}Sr_{1+2x}Mn_2O_7$ samples of $x = 0.5$ and $x = 1$ associated with substantial evolution of the spectral shape. Simulations predict that the pre-edge intensity should increase with Sr

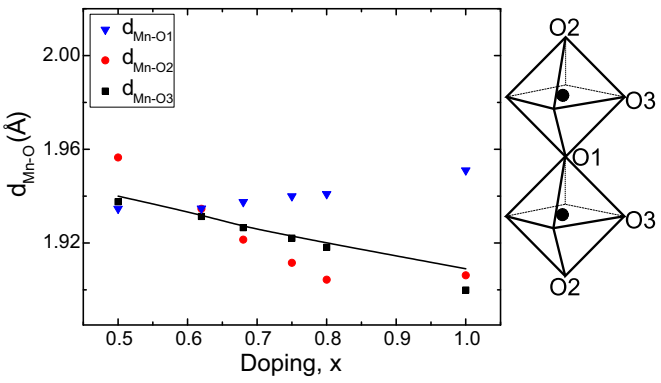

FIG. 2. Mn-O bond lengths d_{Mn-O} in MnO_6 octahedra and the average Mn-O distance $< d_{Mn-O} >$ (black solid line) of $La_{2-2x}Sr_{1+2x}Mn_2O_7$ as a function of doping, x obtained from neutron diffraction [16].

doping. Regarding the postedge, the characteristic broad feature, which is observed at approx. 20 eV above the edge in $LaMnO_3$ [6,7], splits into two in $La_{2-2x}Sr_{1+2x}Mn_2O_7$ samples. We interpret this as a fingerprint of increasing structural anisotropy. The results of calculations are in good qualitative agreement with experimental data.

Since $La_{2-2x}Sr_{1+2x}Mn_2O_7$ with $x = 0$ has not been successfully synthesized, we include spectra of $LaMnO_3$ as a reference for the formal Mn^{3+}. Although it has a different crystal lattice, the local atomic environment is also octahedral. We observe that the absorption edge shifts to higher energies with increasing Sr doping, which we attribute to a decrease of the average Mn-O distance due to a change in the mean valence state of Mn from 3.5+ (for $x = 0.5$) to 4+ (for $x = 1$). Such a correlation of the edge energy with nominal Mn valence state has been observed before in many manganites [5–7,10,11]. The edge energy changes by 1.4 eV between $x = 0.5$ and $x = 1$ samples and by roughly 3 eV between $LaMnO_3$ and $x = 1$ sample (i.e., between formal Mn^{3+} and Mn^{4+}). This edge energy difference is in agreement with that between $LaMnO_3$ and $SrMnO_3$ [20] or between $NdMnO_3$ and $Sr/CaMnO_3$ [13]. Further, we refer to the edge energy shift from its position for $LaMnO_3$ as the chemical shift.

Another characteristic of XANES that significantly evolves upon doping in manganites is the pre-edge area [Fig. 3(b)]. Here we can clearly identify four features denoted as $p1$, $p2$, $p3$, and $p4$. They gradually change with increase of the Mn valence state. The $p1$ is located at roughly 6540 eV and it is the most pronounced for $LaMnO_3$, while for $La_{2-2x}Sr_{1+2x}Mn_2O_7$ samples it is visible only as a shoulder of a more intense $p2$, which shifts to higher energies and strongly increases in intensity with Sr doping. The $p3$ located at roughly 6544.5 eV is barely visible for the $x = 0.5$ sample, but increases in intensity with doping and it is especially well resolved for the $x = 1$ sample. For $LaMnO_3$, there is a clear feature ($p4$) at about 6547–6548 eV, while for $La_{2-2x}Sr_{1+2x}Mn_2O_7$ samples the intensity in this energy range gradually decreases with doping and we observe a steplike behavior for the $x = 1$ sample.

Figure 4 presents results of Mn $K\beta$ CTC and VTC measurements. CTC $K\beta_{1,3}$ and $K\beta'$ lines shift to lower energies and decrease in intensity with doping. For $LaMnO_3$, the $K\beta_{1,3}$ line is located at about 6491 eV and it shifts to lower energy by roughly 0.4 eV for the $x = 1$ sample. We also note that the $K\beta_{1,3}$ line of $LaMnO_3$ has the smallest width, which gradually increases with doping for $La_{2-2x}Sr_{1+2x}Mn_2O_7$ samples, reaching maximum value of 4 eV for the $x = 1$ sample. The intensity of the $K\beta'$ line for $La_{2-2x}Sr_{1+2x}Mn_2O_7$ samples decreases with doping by roughly 15% [see inset of Fig. 4(a)] and by 25% between $LaMnO_3$ and $x = 1$ sample. As for VTC lines shown in Fig. 4(b), $K\beta_{2,5}$ and $K\beta''$ lines for $LaMnO_3$ are observed at the lowest emission energy, and for $La_{2-2x}Sr_{1+2x}Mn_2O_7$ samples both lines move to higher energies with doping and a stronger shift is observed for the $K\beta''$ line (2 eV vs 1 eV for $K\beta_{2,5}$). It is difficult to analyze the intensity changes of VTC lines due to the fact that their background is relatively high and cannot be accurately determined from the spectral range probed. The intensity and linewidth of VTC lines are sensitive to doping, nevertheless, a more quantitative analysis would have a significant uncertainty.

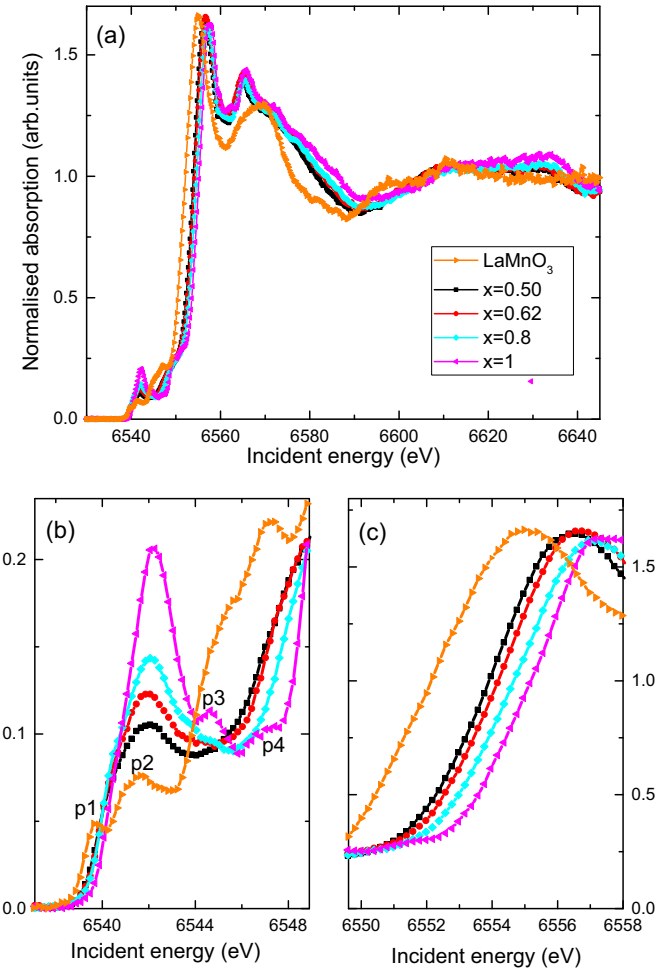

FIG. 3. (a) Normalized $1s3p$ HERFD XANES spectra measured at room temperature for $LaMnO_3$ and selected $La_{2-2x}Sr_{1+2x}Mn_2O_7$ samples. (b) Detailed view of the pre-edge area with four features marked as $p1$, $p2$, $p3$, and $p4$. (c) Detailed view of the absorption edge. Lines are a guide to the eye.

IV. DISCUSSION

A. XANES

We start the discussion with analysis of XANES measurements. The Mn K-edge spectra can be divided into two areas: the main edge, which is due to transitions from the $1s$ core state to the $4p$ continuum and the pre-edge region. The latter is typically attributed to quadrupole transitions from the $1s$ core state to the empty $3d$ states. However, in manganites, additionally we observe signals from the local or nonlocal $3d$ $4p$ wave function mixing, allowing dipole transitions from $1s$ to the $4p$ character of the $3d$ band [24].

In transition metal oxides the pre-edge region typically contains several features, whose origin is still under debate [24]. However, there are several general trends observed is manganese compounds. The first is that the pre-edge centroids for Mn^{2+}, Mn^{3+}, and Mn^{4+} shift toward higher energy with average oxidation state, and the second is that the total intensity of pre-edge area increases with the site distortion and with oxidation state as more empty $3d$ levels are created by the

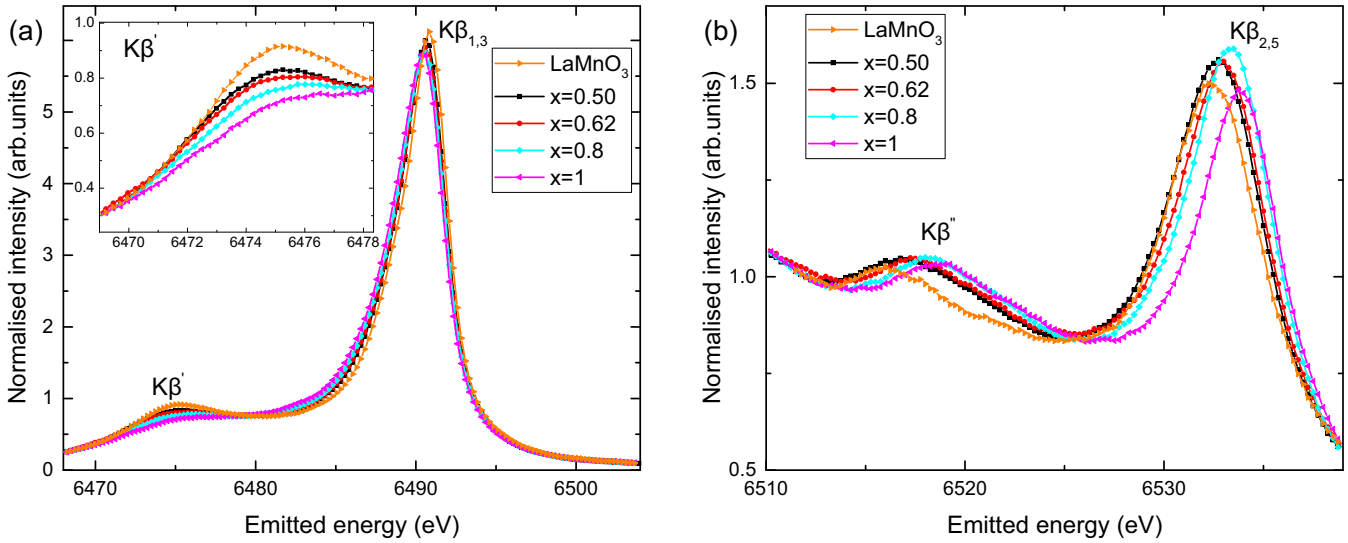

FIG. 4. Normalized Mn $K\beta$ XES spectra. Panel (a) shows CTC transitions ($K\beta'$ and $K\beta_{1,3}$ lines), inset shows detailed view on the $K\beta'$ line. Panel (b) shows VTC transitions ($K\beta''$ and $K\beta_{2,5}$ lines) of $LaMnO_3$ and selected $La_{2-2x}Sr_{1+2x}Mn_2O_7$ samples. Lines connecting points are a guide to the eye.

ionization of Mn [25]. The overall shape of these features is a consequence of quadrupolar and dipolar transitions resulting in overlapping lines and, therefore, single transitions cannot be easily distinguished. In general, there are two types of dipolar transitions: local, i.e., from $1s$ to the $4p$ character of the $3d$ band of the excited ion for geometry with broken inversion symmetry and nonlocal, i.e., to $3d$ states of neighboring metal sites through the oxygen-mediated intersite hybridization Mn($4p$)-O($2p$)-Mn'($3d$) [24,26]. It has been suggested that this nonlocal contribution appears at a higher energy since such a final state is also more delocalized and thus it is less affected by the core hole potential [24,26].

TFY-XANES measurements on $La_{1-x}Sr_xMnO_3$ and $La_{1-x}Sr_{1+x}MnO_4$ showed similar behavior of the pre-edge range, i.e., there were several features present, which were shifting to higher energy upon doping and their intensity was increasing, particularly at the energy range corresponding to the most intense feature [18,20,22]. However, TFY-XANES did not allow for clear distinguishing of pre-edge features. HERFD-XANES measurements presented here provide better resolution and, as a result, we are able to distinguish several distinct features ($p1$, $p2$, $p3$, and $p4$) in the pre-edge range in $La_{2-2x}Sr_{1+2x}Mn_2O_7$. As in other manganites, with increase of Mn^{4+} content the total intensity of the pre-edge increases and the centroid shifts to higher energy [see Fig. 3(b)].

Recent HERFD-XANES study on $TbMn_{1-x}Co_xO_3$ showed two well-resolved features in the pre-edge region at energies corresponding to $p1$ and $p2$ and it has been concluded that $p1$ shows both dipole and quadrupole contributions while $p2$ can be assigned mostly to the nonlocal dipole transition [26]. Particularly interesting was the behavior of the $p2$ feature, which was decreasing in intensity with Co doping even though the content of Mn^{4+} was increasing. This observation was correlated with $4p$-O-$3d$ hybridization, which is strongly reduced when Mn atoms are surrounded by more and more Co^{2+} ($3d^7$) ions instead of Mn^{3+}($3d^4$) or Mn^{4+} ($3d^3$), i.e., the intensity of $p2$ decreases with decreasing the number of empty states in $3d$ orbitals. In our case, the intensity of the $p2$ feature increases with doping, particularly for the $x = 1$ sample containing formal Mn^{4+} ions, which is in agreement with interpretation suggested by Cuartero *et al.* [26]

To obtain more quantitative understanding of the pre-edge doping evolution, we estimated the $p2$ intensity, taken as the maximum from the experimental data [Fig. 5(a)] as well as maximum and area from the data fits (see the supplement [15] and supplemental Fig. 5). In Fig. 5(a), we also show the dependence of the probability of finding a different number of Mn^{4+} ions as neighbors of a given absorber (Mn ion) calculated from a binomial distribution. In a bilayer, there are five possible Mn neighbors, but only four equatorial are equivalent. Mn-O(apical)-Mn distance is different by max. 0.06 Å, which is roughly 1.5% different from Mn-O(equatorial)-Mn distance. The best correlation with the increase of the $p2$ feature intensity follows the probability of all neighbors being Mn^{4+}. Since Mn^{4+} ions have more empty states available on orbitals of e_g symmetry (σ-like) compared to Mn^{3+}, more Mn^{4+} ions as neighbors should make Mn($4p$)-O($2p$)-Mn'($3d$) hybridized states more probable. Our observations not only confirm that the $p2$ feature is mostly of nonlocal dipolar origin, but also provide quantitative experimental evidence that its intensity increase is due to the increase of the number of Mn^{4+} ions.

Without more quantitative support from theory, we cannot make firm conclusions on the origin of $p3$, and $p4$, and other pre-edge features. Such high-energy features have been suggested to also originate from nonlocal hybridized states and were observed, for example, in MnO_2 [25] or in trivalent cobalt oxides [27]. We only note that intensity of $p3$ increases with doping, while intensity around $p4$ decreases and a similar steplike feature, as that visible in $Sr_3Mn_2O_7$, has been also observed, for example, in $SrMnO_3$ [20].

Now we discuss the doping dependence of the main edge, which is predominantly determined by two effects: the changes

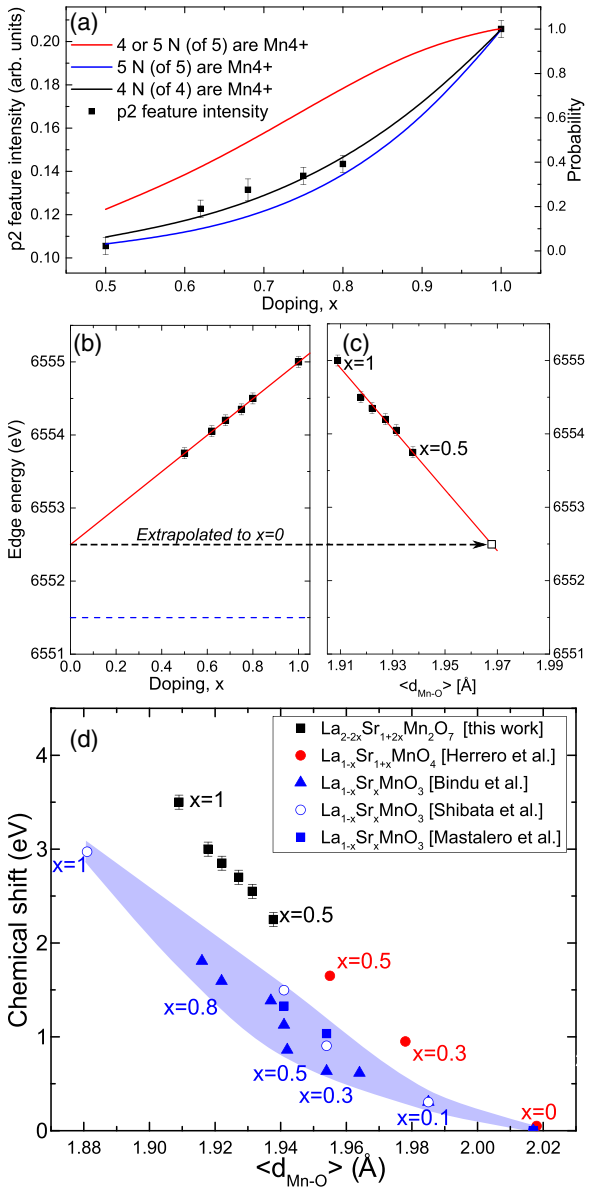

FIG. 5. (a) The intensity of $p2$ feature (points) and probabilities (solid lines) of different numbers of Mn^{4+} neighbors (N) as a function of doping. The edge energy taken as the maximum of the first derivative from TFY XANES as a function of (b) doping and (c) average Mn-O distance $< d_{\mathrm{Mn-O}} >$. Dashed blue line shows the edge energy for $LaMnO_3$, solid red lines are linear fits. Empty black square is the value extrapolated to $La_2SrMn_2O_7$ ($x = 0$). (d) The chemical shift with respect to $LaMnO_3$ for $La_{2-2x}Sr_{1+2x}Mn_2O_7$, $La_{1-x}Sr_xMnO_3$ [20–22], and $La_{1-x}Sr_{1+x}MnO_4$ [18] as a function of $< d_{\mathrm{Mn-O}} >$. All distances are derived from XRD [17] or neutron diffraction [23].

in the Mn $3d$ occupation and the changes in the Madelung potential [28]. In manganites, it has been observed that the edge energy is correlated with the nominal valence state of the Mn ion [5–7,10,11,13,18,26]. Such a trend is a general property of mixed-valence manganese oxides [29]. We find a linear dependance for bilayered manganites as well, which is characterized by the slope of 2.50 ± 0.03 eV per doping level [Fig. 5(b)]. It is smaller than approx. 3 eV per doping level observed for $La_{1-x}Sr_xMnO_3$ [20,22] or $La_{1-x}Sr_{1+x}MnO_4$ [18] and 4 eV per doping level in $La_{1-x}Ca_xMnO_3$ [7]. If this linear trend is extrapolated to lower dopings, for a hypothetical $La_2SrMn_2O_7$ (i.e., $x = 0$) the edge should appear at approx. 1 eV higher energy compared to $LaMnO_3$ (both compounds contain formal Mn^{3+} ions). This is a large value since in very different local environments in crystalline and molecular materials with formal Mn^{3+}, the variation of the edge position is less than 1 eV [29,30]. We come back to this below.

In Fig. 5(d), we present the chemical shift with respect to $LaMnO_3$ for $La_{2-2x}Sr_{1+2x}Mn_2O_7$, $La_{1-x}Sr_xMnO_3$, and $La_{1-x}Sr_{1+x}MnO_4$ as a function of $< d_{\mathrm{Mn-O}} >$. For all three families of Sr-doped manganites, the chemical shift decreases with $< d_{\mathrm{Mn-O}} >$ as expected, since the latter parameter decreases with doping [17,23]. For $La_{1-x}Sr_xMnO_3$, we show results from three studies [20–22], which give slightly different values of the edge energy for the same nominal doping. Nevertheless, one can see that tetragonal families $La_{2-2x}Sr_{1+2x}Mn_2O_7$ and $La_{1-x}Sr_{1+x}MnO_4$ are located to the right from $La_{1-x}Sr_xMnO_3$. The biggest values of the chemical shift for a given doping are found for $La_{2-2x}Sr_{1+2x}Mn_2O_7$ family. The data of $La_{2-2x}Sr_{1+2x}Mn_2O_7$ compounds appear to continue the trend observed for $La_{1-x}Sr_{1+x}MnO_4$ samples, however, there is a gap between $x = 0.5$ samples.

For compounds with given doping (the same nominal valence of Mn) of different families, one could expect the same contribution from Mn occupation to the edge energy. Since the contribution from Madelung potential depends on the interionic distances, one could anticipate a monotonic dependence between the chemical shift and $< d_{\mathrm{Mn-O}} >$. However, there is no apparent trend between the chemical shift and $< d_{\mathrm{Mn-O}} >$ for a given doping, which confirms that contributions from the electronic occupation and the local structure to the XANES spectra cannot be simply separated [31].

It is known that for the $La_{1-x}Ca_xMnO_3$ family, XANES spectra of the doped compounds cannot be obtained by a simple weighted sum of $LaMnO_3$ and $CaMnO_3$ [31,32] due to different crystal and local structures. Nevertheless, the spectra of doped compounds can be well reproduced if one takes weighted spectra of doped compounds with a similar local environment [31]. We observe the same behavior for the $La_{2-2x}Sr_{1+2x}Mn_2O_7$ family (see the supplement [15] and supplemental Fig. 6). The edge and pre-edge shape as well as edge position of the spectra of $x = 0.5$ and $x = 0.75$ compounds cannot be reproduced by a weighted sum of $Sr_3Mn_2O_7$ with $LaMnO_3$ and $Sr_3Mn_2O_7$ with $La_2SrMn_2O_7$, respectively, but they can if one uses weighted sums of spectra of other mixed valence samples, which have similar local structure.

B. XES

The Mn $K\beta$ XES spectra (Fig. 4) consist of CTC and VTC lines. There are two CTC spectral features, both arising from $3p \rightarrow 1s$ decay process: a strong $K\beta_{1,3}$ peak and a broader $K\beta'$ shoulder at lower emitted energy [33]. Strong spin selectivity of CTC transitions makes them sensitive to the net spin $3d$ moment [34]. In manganese oxides, Mn is always in a high spin configuration. Therefore, a change in the Mn spin directly reflects a change of the charge on Mn [33]. With decrease of the net spin (increase of the charge on Mn) the $K\beta_{1,3}$ line

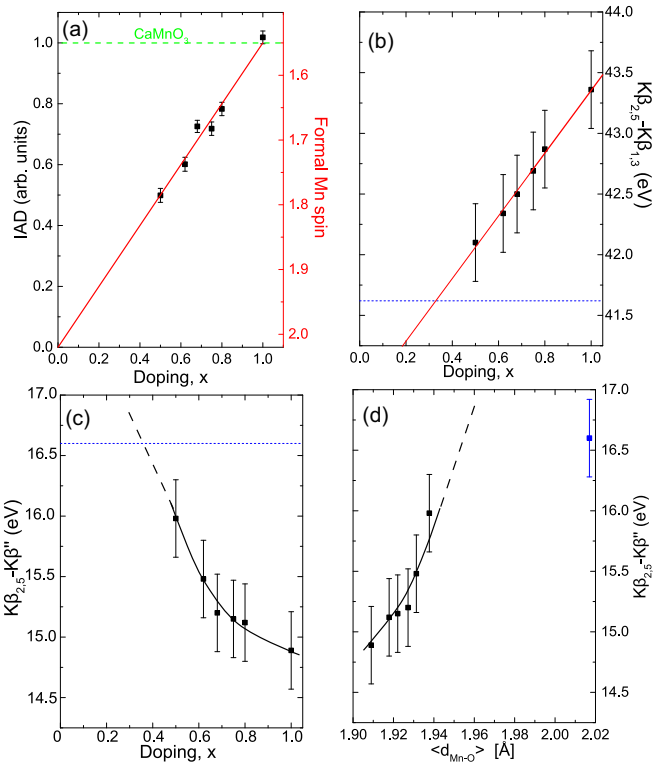

FIG. 6. (a) Integrated absolute difference (IAD) of $La_{2-2x}Sr_{1+2x}Mn_2O_7$ samples with respect to $LaMnO_3$ (IAD = 0) and $CaMnO_3$ (IAD = 1, green dashed line), and a nominal Mn spin (solid red line) as a function of doping. (b) Energy difference $K\beta_{2,5} - K\beta_{1,3}$ as a function of doping (red solid line is a linear fit to the data). Energy difference $K\beta_{2,5} - K\beta''$ as a function of doping [panel (c)] and $< d_{Mn-O} >$ [panel (d)]. Dashed blue lines and the blue data point indicate the value for $LaMnO_3$; solid and dashed black lines are guides to the eye.

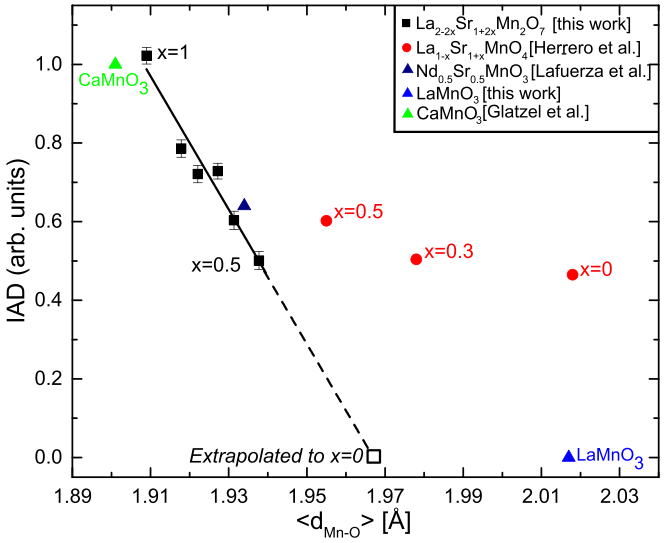

FIG. 7. Normalized IAD for $La_{2-2x}Sr_{1+2x}Mn_2O_7$, $La_{1-x}Sr_{1+x}MnO_4$ [39], and $Nd_{0.5}Sr_{0.5}MnO_3$ [13] with respect to $LaMnO_3$ (IAD = 0) and $CaMnO_3$ (IAD = 1) [12,48]. Black empty square indicates the value extrapolated to $La_2SrMn_2O_7$ ($x = 0$). Solid black line is a linear fit to data for $La_{2-2x}Sr_{1+2x}Mn_2O_7$ samples.

shifts to lower energy and the $K\beta'$ line decreases in intensity [8,12,33,35]. We observe it also for $La_{2-2x}Sr_{1+2x}Mn_2O_7$ [see Fig. 4(a)]. The change of $K\beta_{1,3}$ energy between $LaMnO_3$ and $Sr_3Mn_2O_7$ ($x = 1$), which amounts to 0.4 eV, is the same as between $NdMnO_3$ and $SrMnO_3$ [13] or Mn^{2+} and Mn^{3+} mononuclear complexes [36]. In fact, the energy of the $K\beta_{1,3}$ line decreases linearly with doping and this dependence extrapolates to the energy of $LaMnO_3$ at $x = 0$ [see the supplement [15] and supplemental Fig. 7(a)].

To perform quantitative analysis of the CTC spectra, we used the method of integrated absolute difference (IAD) [37,38]. The IAD values calculated for $La_{2-2x}Sr_{1+2x}Mn_2O_7$ samples with respect to the reference spectra of $LaMnO_3$ and $CaMnO_3$ are plotted as a function of doping in Fig. 6(a). We see that IAD depends linearly on doping (formal Mn valence). Upon comparison with IAD values obtained for other Mn oxides, namely MnO ($S = 5/2$), Mn_2O_3 ($S = 2$), and MnO_2 ($S = 3/2$), we can study the evolution of Mn spin and thus charge [12]. The change of IAD between the $x = 1$ and $x = 0.5$ samples is roughly half of that between $CaMnO_3$ and $LaMnO_3$, indicating that doping affects mostly charge on Mn ions. Such an IAD dependence on Mn formal valence was observed in some Mn oxides or undoped manganites (e.g., $LaMnO_3$ and $CaMnO_3$) [12]. However, it is in contrast to behavior observed for single-layer $La_{1-x}Sr_{1+x}MnO_4$, where almost identical IAD values are observed in the broad doping range [39]. This was attributed to localization of doped charge (holes) on oxygen rather than on Mn. In Fig. 7, we compare IAD values for single, bilayered, and pseudocubic manganites. It is clear that Sr doping of bilayerd manganites affects the shape of CTC $K\beta$ spectra more than in the case of single-layered materials. It is likely related to negligible MnO_6 octahedra distortion (see the supplement [15] and supplemental Fig. 2) and thus the nearly uniform occupation variation of all $3d$ e_g Mn orbitals upon doping. This is in contrast to the single-layer family, where doping mainly affects the occupancy of (apical) oxygen orbitals at nearly constant charge of Mn ions [39].

The width of the $K\beta_{1,3}$ line is the smallest for $LaMnO_3$, for $La_{2-2x}Sr_{1+2x}Mn_2O_7$ samples it increases with doping [see the supplement and supplemental Fig. 7(b)]. This effect could be caused by the crystal field splitting that affects the shape and width of the experimentally measured lines. The crystal field splitting will increase with decrease of the average Mn-O distance (i.e., with increase of doping), which can explain the observed line broadening. Similar doping effect was observed for oxygen-K electron energy-loss lines in $La_{1-x}Ca_xMnO_3$ [40]. Since $K\beta_{1,3}$ is predominantly formed by a set of multiplets, an extensive modeling within the crystal-field multiplet theory [33,41] would be required to fully understand the origin of this effect.

VTC lines arise from transitions from occupied orbitals located a few eV below the Fermi level, i.e., from the valence band, which contains mixed metal-ligand states of metal p-character, to $1s$ [35]. It has been shown that the $K\beta''$ line corresponds to transitions from valence electronic levels with strong s-ligand character while the $K\beta_{2,5}$ line has strong ligand p contribution [42,43]. In contrast to the $K\beta_{1,3}$ line, VTC lines shift to higher energies with doping [Fig. 4(b)] and their

maxima do not show a linear dependence, which extrapolates to $LaMnO_3$ for $x = 0$ [see the supplement [15] and supplemental Fig. 7(a)], indicating that the local structure affects VTC lines. Similar shift of VTC lines with doping was also observed between $NdMnO_3$ and $SrMnO_3$ ($CaMnO_3$) [13]. Also, for Cr compounds, the energy of VTC lines was increasing with oxidation [44,45].

In Fig. 6(b), we show the energy difference $K\beta_{2,5} - K\beta_{1,3}$, as a function of doping. Despite significant uncertainty, we observe a clear linear dependence. Such a difference was shown to increase with the formal oxidation state of $3d$ transition-metal ions [46]. Based on results for many different Mn compounds, the average value of $K\beta_{2,5} - \mathrm{K}\beta_{1,3}$ was deduced to increase linearly by about 1.3 eV per oxidation unit [46]. In the case of $La_{2-2x}Sr_{1+2x}Mn_2O_7$, we find it to be two times larger, which indicates much stronger modification of Mn ionic potentials upon hole doping than typically observed in manganese oxides.

The energy difference $K\beta_{2,5} - K\beta''$ reflects the energy separation between molecular orbitals with ligand s and p character [42,43], which usually correlates with the atomic number of the ligand and thus it is used to identify ligands [46]. However, little is known on the doping dependence and, to our knowledge, there are no such studies concerning manganites. It has been shown that in transition-metal oxides, the $K\beta_{2,5} - K\beta''$ separation typically is of about 15–16 eV and a similar value can be deduced from XPS measurements on $x = 0.4$ $La_{2-2x}Sr_{1+2x}Mn_2O_7$ sample [47]. This is what we also observe in VTC spectra shown in Figs. 6(c) and 6(d). Moreover, such high-resolution spectra show that this difference systematically decreases with doping, reaching approx. 15 eV at $x = 1$. It indicates that the doping changes ligand orbitals of s character more than the p ones. From $K\beta_{2,5} - K\beta''$ as a function of $< d_{\mathrm{Mn-O}} >$ [Fig. 6(c)], one could conclude that the value expected for $x = 0$ would likely be significantly different than that for $LaMnO_3$. This is expected since the $K\beta_{2,5}$ line strongly depends on the metal's local symmetry [35,42].

Overall, XANES and XES parameters, which depend on the local structure, show such doping dependence that their extrapolation to a hypothetical $La_2SrMn_2O_7$ ($x = 0$) would result in significantly different values than that observed for $LaMnO_3$. These are the doping dependencies of the edge position [Fig. 5(a)], energy of $K\beta_{2,5}$ and $K\beta''$ [see the supplement [15] and supplemental Fig. 7(a)], and energy differences between XES lines [Figs. 6(b) and 6(c)]. At the first sight, one might think that this is obviously due to the fact that $LaMnO_3$ has a very different type of crystal and local structure (distortion of MnO_6 octahedra). However, single-layer $LaSrMnO_4$ has a tetragonal structure as bilayered compounds, but has the edge energy almost the same as $LaMnO_3$ [18]. It indicates that crystal-structure evolution (Mn-O distances) in bilayered manganites is affected by hole doping less than in other families. On the other hand, the local Mn charge in a bilayered family evolves in agreement with a trend set by $LaMnO_3$ and $CaMnO_3$ [Fig. 6(a)].

All these observations are revealed by the dependence of the edge energy and IAD plotted as a function of $< d_{\mathrm{Mn-O}} >$, which provides an estimation of the expected average Mn-O distance for $x = 0$ bilayered compound. Extrapolations shown in Figs. 5(c) and 7 indicate $< d_{\mathrm{Mn-O}} > \approx 1.97(1)$. However, a structure with such small $< d_{\mathrm{Mn-O}} >$ is unlikely to be realized, taking into account ionic radii of sixfold coordinated formal Mn^{3+} (0.645 Å) and twofold coordinated O^{2-} (1.35 Å). On the other hand, single-layer $La_{1-x}Sr_{1+x}MnO_4$ *can be* synthesized from $x = 0$, but such a compound is strongly elongated along c axis resulting, in very strong distortion (see the supplement [15] and supplemental Fig. 2) and $< d_{\mathrm{Mn-O}} >$ of about 2.02 Å, which is nearly identical to that in $LaMnO_3$. The main difference between these systems is related to structural anisotropy. In single-layer compounds, the distortion of MnO_6 octahedra is static, while in the pseudocubic manganites the dynamic Jahn-Teller effect is present. Nevertheless, both compounds exhibit nearly identical Mn K-edge energy, which is significantly different than expected for $x = 0$ bilayered manganite. Upon comparison of IAD between these families and the bilayered one, characterized by nondistorted octahedra, we can deduce that local charge transfer from Mn toward oxygen is enhanced by static distortion. Provided that lattice can accommodate such distortion (anisotropic charge distribution), the compound might be stable. Apparently, it is not the case of the bilayered family, where simultaneous distortion and charge transfer are not possible in the rigid crystal structure. We suggest that this is the reason why the $La_{2-2x}Sr_{1+2x}Mn_2O_7$ family can be synthesized only starting from $x = 0.3$ [16]. These observations indicate that there is an intimate relation between the $< d_{\mathrm{Mn-O}} >$ and the localized Mn charge, which enables a formation of stable structures.

V. CONCLUSIONS

The Mn K-edge x-ray absorption spectra of bilayered manganites show doping dependence, which is similar to other manganites and manganese oxides, e.g., the shift of edge energy and the evolution of pre-edge features. However, the absolute values of the chemical shift are bigger in a $La_{2-2x}Sr_{1+2x}Mn_2O_7$ family compared to other manganese perovskites with La and Sr. $K\beta$ x-ray emission spectra show even more significant differences. Mn spin, and thus the localized charge, changes linearly with doping, which is in contrast to single-layer $La_{1-x}Sr_{1+x}MnO_4$. Since XANES and XES probe simultaneously the local structure and electronic properties, we were able to explain why bilayered manganese perovskites cannot be synthesized in the entire Sr doping range. Our results show that for low doping ($x < 0.3$), the expected Mn charge and the average Mn-O distances would correspond to structures, which cannot be realized. We assume that such analysis could be applied to other transition-metal oxide families to assist in prediction of their structural stability upon, e.g., chemical doping or external pressure.

ACKNOWLEDGMENTS

This paper was (partially) supported by the Faculty of Physics and Applied Computer Science, AGH University of Science and Technology, Statutory Task No. 11.11.220.01/6 within a subsidy of the Ministry of Science and Higher Education, Republic of Poland. Access to ESRF was supported by Ministry of Science and Higher Education, Republic of Poland (DIR/WK/2016/19). Assistance provided by ID26 (ESRF) staff was greatly appreciated. M.S. acknowledges

support from the National Science Centre of Poland (Grant No. 2014/14/E/ST3/00026). Work in the Materials Science Division of Argonne National Laboratory (crystal growth and characterization) was sponsored by the US Department of Energy, Office of Science, Basic Energy Sciences, Materials Science and Engineering Division.

[1] Y. Wang, Y. Xie, H. Sun, J. Xiao, H. Cao, and S. Wang, Catal. Sci. Technol. **6**, 2918 (2016).
[2] M. Kubicek, A. H. Bork, and J. L. M. Rupp, J. Mater. Chem. A **5**, 11983 (2017).
[3] J. F. Mitchell, D. N. Argyriou, A. Berger, K. E. Gray, R. Osborn, and U. Welp, J. Phys. Chem. B **105**, 10731 (2001).
[4] D. Rybicki, C. Kapusta, W. Tokarz, H. Štěpánková, V. Procházka, J. Haase, Z. Jirák, D. T. Adroja, and J. F. Mitchell, Phys. Rev. B **78**, 184428 (2008).
[5] Q. Qian, T. A. Tyson, C.-C. Kao, M. Croft, S.-W. Cheong, G. Popov, and M. Greenblatt, Phys. Rev. B **64**, 024430 (2001).
[6] M. Croft, D. Sills, M. Greenblatt, C. Lee, S.-W. Cheong, K. V. Ramanujachary, and D. Tran, Phys. Rev. B **55**, 8726 (1997).
[7] G. Subías, J. García, M. G. Proietti, and J. Blasco, Phys. Rev. B **56**, 8183 (1997).
[8] T. A. Tyson, Q. Qian, C.-C. Kao, J.-P. Rueff, F. M. F. de Groot, M. Croft, S.-W. Cheong, M. Greenblatt, and M. A. Subramanian, Phys. Rev. B **60**, 4665 (1999).
[9] F. Bridges, C. H. Booth, G. H. Kwei, J. J. Neumeier, and G. A. Sawatzky, Phys. Rev. B **61**, R9237 (2000).
[10] C. H. Booth, F. Bridges, G. H. Kwei, J. M. Lawrence, A. L. Cornelius, and J. J. Neumeier, Phys. Rev. Lett. **80**, 853 (1998).
[11] M. Sikora, C. Kapusta, K. Knížek, Z. Jirák, C. Autret, M. Borowiec, C. J. Oates, V. Procházka, D. Rybicki, and D. Zajac, Phys. Rev. B **73**, 094426 (2006).
[12] P. Glatzel, T.-S. Weng, K. Kvashnina, J. Swarbrick, M. Sikora, E. Gallo, N. Smolentsev, and R. A. Mori, J. Electron. Spectrosc. Relat. Phenom. **188**, 17 (2013).
[13] S. Lafuerza, J. García, G. Subías, J. Blasco, and P. Glatzel, Phys. Rev. B **93**, 205108 (2016).
[14] J. E. Millburn, J. F. Mitchell, and D. N. Argyriou, Chem. Commun. **15**, 1389 (1999).
[15] See Supplemental Material at http://link.aps.org/supplemental/10.1103/PhysRevB.97.115158 for additional details of sample characterization, data analysis, and supplemental figures.
[16] C. D. Ling, J. E. Millburn, J. F. Mitchell, D. N. Argyriou, J. Linton, and H. N. Bordallo, Phys. Rev. B **62**, 15096 (2000).
[17] R. Bindu, Eur. Phys. J. B **37**, 321 (2004).
[18] J. Herrero-Martín, J. García, G. Subías, J. Blasco, and M. C. Sánchez, Phys. Rev. B **72**, 085106 (2005).
[19] O. Bunau and Y. Joly, J. Phys.: Condens. Matter **21**, 345501 (2009).
[20] T. Shibata, B. A. Bunker, and J. F. Mitchell, Phys. Rev. B **68**, 024103 (2003).
[21] V. R. Mastelaro, D. P. F. de Souza, and R. A. Mesquita, X-Ray Spectrom. **31**, 154 (2002).
[22] R. Bindu, S. K. Pandey, A. Kumar, S. Khalid, and A. V. Pimpale, J. Phys.: Condens. Matter **17**, 6393 (2005).
[23] D. Senff, P. Reutler, M. Braden, O. Friedt, D. Bruns, A. Cousson, F. Bourée, M. Merz, B. Büchner, and A. Revcolevschi, Phys. Rev. B **71**, 024425 (2005).
[24] F. de Groot, G. Vanko, and P. Glatzel, J. Phys.: Condens. Matter **21**, 104207 (2009).
[25] F. Farges, Phys. Rev. B **71**, 155109 (2005).
[26] V. Cuartero, S. Lafuerza, M. Rovezzi, J. Garcia, J. Blasco, G. Subias, and E. Jimenez, Phys. Rev. B **94**, 155117 (2016).
[27] G. Vanko, F. de Groot, S. Huotari, R. J. Cava, R, T. Lorenz, and M. Reuther, arXiv:0802.2744.
[28] A. H. de Vries, L. Hozoi, and R. Broer, Int. J. Quantum Chem. **91**, 57 (2003).
[29] A. Manceau, M. Marcus, and S. Grangeon, Amer. Miner. **97**, 816 (2012).
[30] T.-C. Weng, W.-Y. Hsieh, E. S. Uffelman, S. W. Gordon-Wylie, T. J. Collins, V. L. Pecoraro, and J. E. Penner-Hahn, J. Am. Chem. Soc. **126**, 8070 (2004).
[31] J. Garcia, G. Subias, V. Cuartero, and J. Herrero-Martin, J. Synchrotron Radiat. **17**, 386 (2010).
[32] J. Chaboy, J. Synchrotron Radiat. **16**, 533 (2009).
[33] G. Peng, F. M. F. deGroot, K. Haemaelaeinen, J. A. Moore, X. Wang, M. M. Grush, J. B. Hastings, D. P. Siddons, W. H. Armstrong, O. C. Mullins, and S. P. Cramer, J. Am. Chem. Soc. **116**, 2914 (1994).
[34] P. Glatzel and U. Bergmann, Coord. Chem. Rev. **249**, 65 (2005).
[35] M. Rovezzi and P. Glatzel, Semicond. Sci. Technol. **29**, 023002 (2014).
[36] M. A. Beckwith, M. Roemelt, M.-N. Collomb, C. DuBoc, T.-C. Weng, U. Bergmann, P. Glatzel, F. Neese, and S. DeBeer, Inorg. Chem. **50**, 8397 (2011).
[37] J. P. Rueff, A. Shukla, A. Kaprolat, M. Krisch, M. Lorenzen, F. Sette, and R. Verbeni, Phys. Rev. B **63**, 132409 (2001).
[38] G. Vanko, J.-P. Rueff, A. Mattila, Z. Nemeth, and A. Shukla, Phys. Rev. B **73**, 024424 (2006).
[39] J. Herrero-Martín, A. Mirone, J. Fernández-Rodríguez, P. Glatzel, J. García, J. Blasco, and J. Geck, Phys. Rev. B **82**, 075112 (2010).
[40] W. Luo, M. Varela, J. Tao, S. J. Pennycook, and S. T. Pantelides, Phys. Rev. B **79**, 052405 (2009).
[41] J. Kawai, M. Takami, and C. Satoko, Phys. Rev. Lett. **65**, 2193 (1990).
[42] G. Smolentsev, A. V. Soldatov, J. Messinger, K. Merz, T. Weyhermüller, U. Bergmann, Y. Pushkar, J. Yano, V. K. Yachandra, and P. Glatzel, J. Am. Chem. Soc. **131**, 13161 (2009).
[43] E. Gallo and P. Glatzel, Adv. Mater. **26**, 7730 (2014).
[44] S. G. Eeckhout, O. V. Safonova, G. Smolentsev, M. Biasioli, V. A. Safonov, L. N. Vykhodtseva, M. Sikora, and P. Glatzel, J. Anal. At. Spectrom. **24**, 215 (2009).
[45] S. Fazinic, L. Mandic, M. Kavcic, and I. Bozicevic, Spectrochim. Acta, Part B **66**, 461 (2011).
[46] S. Fazinic, L. Mandic, M. Kavcic, and I. Bozicevic, J. Anal. At. Spectrom. **26**, 2467 (2011).
[47] H. Fujiwara, A. Sekiyama, H. Sugiyama, G. Funabashi, T. Muro, A. Higashiya, M. Yabashi, K. Tamasaku, T. Ishikawa, S. Miyasaka, H. Nakamura, T. Kimura, Y. Tokura, and S. Suga, J. Phys. Soc. Jpn. **81**, SB069 (2012).
[48] J. Blasco, C. Ritter, J. García, J. M. de Teresa, J. Pérez-Cacho, and M. R. Ibarra, Phys. Rev. B **62**, 5609 (2000).